Discrete reduced-symmetry solitons and second-band vortices in two-dimensional nonlinear waveguide arrays

Magnus Johansson,[1,2,3,*] Andrey A. Sukhorukov,[1,†] and Yuri S. Kivshar[1,‡]

[1]*Nonlinear Physics Centre, Research School of Physics and Engineering, Australian National University, Canberra, Australian Capital Territory 0200, Australia*
[2]*Department of Physics, Chemistry and Biology (IFM), Linköping University, SE-581 83 Linköping, Sweden*
[3]*School of Pure and Applied Natural Sciences, University of Kalmar, SE-391 82 Kalmar, Sweden*

Considering a two-dimensional lattice of weakly coupled waveguides, where each waveguide may carry two orthogonal modes of *dipolar* character, we present a nonlinear discrete vector model for the study of Kerr optical solitons with profiles having a reduced symmetry relative to the underlying lattice. We describe analytically and numerically existence and stability properties of such states in square and triangular lattices and also reveal directional mobility properties of two-dimensional gap solitons which were recently observed in experiment. The model also describes one-site peaked discrete vortices corresponding to experimentally observed "second-band" vortex lattice solitons, for which oscillatory instabilities are predicted. We also introduce a concept of "rotational Peierls-Nabarro barrier" characterizing the minimum energy needed for rotation of stable dipole modes and compare numerically translational and rotational energy barriers in regimes of good mobility.

PACS number(s): 05.45.Yv, 42.65.Tg, 42.65.Wi, 42.82.Et

I. INTRODUCTION

Periodic photonic structures offer novel possibilities to control the propagation of optical waves in the form of nonlinear localized modes or solitons. In particular, it was theoretically predicted in [1,2] that two-dimensional (2D) square and triangular nonlinear photonic band-gap structures may, in addition to the well-known fundamental gap solitons having the same symmetry as the lattice itself, also support stable solitary waves with lower symmetry. Such solutions were found to bifurcate, e.g., from an X point in the first Brillouin zone, corresponding to a band edge of the *second* linear dispersion band, and the breaking of the discrete lattice rotational symmetry appears due to the anisotropic nature of the dispersion curve at this point. Recently, reduced-symmetry gap solitons were also observed experimentally in optically induced square [3] and triangular [4] photonic lattices. For square lattices, they were found to exhibit strong anisotropy also in their mobility properties, being highly mobile in one direction and trapped in the other, while for triangular lattices, no mobility was observed.

In addition, recently, it was predicted [5] and experimentally verified [6] that excitation of a coherent superposition of two degenerate modes of the second linear band in a square lattice, associated with points X and X' (90° rotated with respect to X) in the Brillouin zone and phase-shifted by $\pi/2$, could result in stable localized vortex solitons with the phase structure of a 2D array of vortices with alternating rotation between neighboring sites. However, the original theoretical analysis in Refs. [1,2] was done using the assumption of slowly varying envelopes, which can be justified only close to the linear band when the soliton has small amplitude and extends over many lattice sites, so that pure discreteness effects can be neglected. However, in experiments [3,4,6] strongly localized modes were observed, and to correctly describe their properties (such as stability, mobility, etc.), proper account of the discrete nature of their envelopes should be taken. More recent theoretical studies [3,4,7] used numerical techniques to continue small-amplitude solutions with continuous envelopes into families of solitary waves bifurcating from band edges, ending in solutions localized almost at single lattice sites. Very recently, the persistence of localized gap solitons beyond the small-amplitude limit has also been rigorously proven for a class of separable symmetric potentials [8].

In this work, we will use an opposite, "anticontinuous," approach for describing second-band solitons in 2D lattices by continuation of single waveguide modes. We introduce a set of coupled lattice equations, derived using coupled-mode theory with the assumption that each individual 2D waveguide may carry two degenerate modes of *dipolar* character, corresponding to the symmetry of the X and X' points, respectively.

The structure of this paper is as follows. In Sec. II, we derive the general coupled-mode equations accounting for linear and nonlinear couplings between the dipole modes of optical waveguides. We use this model to first consider the nonlinear modes of a single waveguide in Sec. III. Then, we perform the detailed classification and analysis of solitons in square and triangular lattices in Secs. IV and V, respectively. We study the mobility of such solitons in Sec. VI. Finally, we summarize our findings in Sec. VII.

─────────
*Electronic address: mjn@ifm.liu.se; http://people.ifm.liu.se/majoh

†Electronic address: ans124@physics.anu.edu.au; http://physics.anu.edu.au/nonlinear

‡Electronic address: ysk124@physics.anu.edu.au; http://physics.anu.edu.au/nonlinear

II. GENERAL MODEL

Consider a single 2D waveguide with two modes $\Psi_a(x,y)$ and $\Psi_b(x,y)$ corresponding to the same propagation constant k,

$$-k\Psi_{a,b} + D\frac{\partial^2\Psi_{a,b}}{\partial x^2} + D\frac{\partial^2\Psi_{a,b}}{\partial y^2} + V(x,y)\Psi_{a,b} = 0, \quad (1)$$

where $V(x,y) \equiv V_s(x,y)$ is the normalized refractive index profile for a single waveguide. We normalize the mode profiles, $\int dx dy |\Psi_{a,b}|^2 = 1$.

We now consider a lattice consisting of coupled waveguides with $V = \Sigma_m V_s(x - x_m, y - y_m)$ and present the total field as a sum of modes: $\Psi = \Sigma_m [A_m \Psi_a(x,y) + B_m \Psi_b(x,y)]\exp(ikz)$. Assuming that the modes are weakly overlapping and taking into account nonlinear interaction of modes at the same waveguide only, we obtain a set of coupled equations for the mode amplitudes

$$i\frac{dA_m}{dz} + \sum_j C_{m,j}^{AA} A_j + \sum_j C_{m,j}^{AB} B_j + \gamma_A |A_m|^2 A_m + \sigma(2|B_m|^2 A_m$$
$$+ B_m^2 A_m^*) = 0,$$

$$i\frac{dB_m}{dz} + \sum_j C_{m,j}^{BA} A_j + \sum_j C_{m,j}^{BB} B_j + \gamma_B |B_m|^2 B_m + \sigma(2|A_m|^2 B_m$$
$$+ A_m^2 B_m^*) = 0. \quad (2)$$

Here, $C_{m,m} \equiv 0$,

$$C_{m,j}^{AA} = \int dx dy \Psi_a(x - x_m, y - y_m)V(x - x_m, y - y_m)\Psi_a(x - x_j, y - y_j),$$

$$C_{m,j}^{BB} = \int dx dy \Psi_b(x - x_m, y - y_m)V(x - x_m, y - y_m)\Psi_b(x - x_j, y - y_j),$$

$$C_{m,j}^{AB} = \int dx dy \Psi_a(x - x_m, y - y_m)V(x - x_m, y - y_m)\Psi_b(x - x_j, y - y_j).$$

It can be proved that $C_{m,j} \equiv C_{j,m}$ and $C_{m,j}^{AB} = C_{m,j}^{BA}$. For an isotropic Kerr-type nonlinearity,

$$\gamma_A = \pm \int dx dy |\Psi_a(x,y)|^4,$$

$$\gamma_B = \pm \int dx dy |\Psi_b(x,y)|^4,$$

and

$$\sigma = \pm \int dx dy |\Psi_a(x,y)|^2 |\Psi_b(x,y)|^2,$$

where the upper (lower) sign describes a self-focusing (self-defocusing) medium. Then, it also follows that $0 \le |\sigma|$
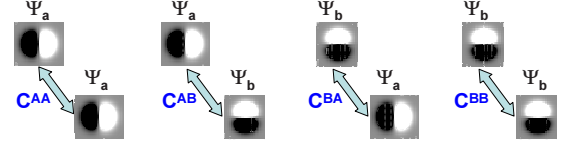

FIG. 1. (Color online) Schematic illustration of coupling between the dipole modes with amplitude profiles Ψ_a and Ψ_b, characterized by the coupling coefficients C^{AA}, C^{AB}, C^{BA}, and C^{BB}.

$\le \frac{1}{2}(|\gamma_A| + |\gamma_B|)$. We present a schematic illustration of dipole modes and their coupling in Fig. 1.

Note that in deriving Eq. (2), no explicit assumptions were made regarding the geometry of the lattice, the geometry of the waveguides, or the nature of the modes, more than that the symmetry has to be sufficiently high to sustain two orthogonal degenerate modes. The appropriate geometrical structure is obtained by specifying the parameters C, γ, and σ, as illustrated below for several explicit examples, which are analyzed in some details.

III. SOLITONS AND VORTICES IN A SINGLE WAVEGUIDE

For a single waveguide, all coupling parameters $C \equiv 0$. As we wish to describe solutions associated with the second linear dispersion band for the full lattice, we choose the two individual waveguide modes Ψ_a and Ψ_b to have a *dipolar* structure, with either a vertical or horizontal nodeline through the waveguide center. From now, we will assume that Ψ_a describes a mode with horizontal dipole moment and Ψ_b a mode with vertical dipole moment (both directions perpendicular to the longitudinal propagation direction z). For example, if the single waveguide is circularly symmetric, then the guided modes have the form $\Psi_a = \cos(\varphi)\psi(r)$ and $\Psi_b = \sin(\varphi)\psi(r)$, where (r,φ) are polar coordinates. It then follows that $\gamma_A = \gamma_B \equiv \gamma$ and $\sigma = \gamma/3$. As another example, we may consider a square waveguide (sidelength L) and $\Psi_a \sim \sin\frac{2\pi x}{L}\sin\frac{\pi y}{L}$, $\Psi_b \sim \sin\frac{\pi x}{L}\sin\frac{2\pi y}{L}$, which again yields $\gamma_A = \gamma_B \equiv \gamma$ but $\sigma = \frac{4}{9}\gamma$. We will from now assume generally that the waveguides and modes have sufficient symmetry to yield $\gamma_A = \gamma_B \equiv \gamma$ and consider the waveguide geometry to be specified by the parameter $\sigma' \equiv \sigma/\gamma$ taking values between 0 and 1.

For a single waveguide with generic σ/γ, there are three fundamental types of stationary solutions:

(I) "Single-mode" dipoles: $A = \sqrt{\beta/\gamma}\exp(i\beta z)$, $B = 0$; or $A = 0$, $B = \sqrt{\beta/\gamma}\exp(i\beta z)$. These correspond to dipole moments pointing in the horizontal and vertical directions, respectively.

(II) "Mixed-mode" dipoles: $A = \pm B = \sqrt{\beta/(\gamma + 3\sigma)}\exp(i\beta z)$. These correspond to dipole moments pointing in the two diagonal directions.

(III) Vortices: $A = \pm iB = \sqrt{\beta/(\gamma + \sigma)}\exp(i\beta z)$, where the two signs correspond to positive and negative charges.

However, in the particular case with $\sigma/\gamma = 1/3$ (circularly symmetric waveguide), the dipole soliton for a single waveguide has an arbitrary orientation, so that there is a continuous family of solutions interpolating between the single-

mode and mixed-mode dipoles and characterized by the angle α: $A = \sqrt{\beta/\gamma}\cos(\alpha)\exp(i\beta z)$, $B = \sqrt{\beta/\gamma}\sin(\alpha)\exp(i\beta z)$.

As is well known, the stability of these solutions depends on the value of the parameter σ' (see, e.g., [9] and references therein and [10–12] for recent results on related models). Performing a standard linear stability analysis, we consider small perturbations $(\epsilon^{(A)}, \epsilon^{(B)})$ to the above exact stationary solutions $[A^{(0)}\exp(i\beta z), B^{(0)}\exp(i\beta z)]$ by writing $A = (A^{(0)} + \epsilon^{(A)})\exp(i\beta z)$, $B = (B^{(0)} + \epsilon^{(B)})\exp(i\beta z)$. Expressing $\epsilon^{(A)} = c\exp(-i\omega z) + d^*\exp(i\omega^* z)$, $\epsilon^{(B)} = f\exp(-i\omega z) + g^*\exp(i\omega^* z)$, and linearizing yields a 4×4 eigenvalue problem for the perturbation eigenvectors $(c, d, f, g)^T$ and eigenfrequencies ω (cf., e.g., [12] for the detailed structure of the matrix). Due to the overall gauge invariance, $\omega = 0$ is always a doubly degenerate eigenvalue, so the linear stability is determined by the remaining two eigenvalues. These are given by:

(I) Single-mode dipoles: $\omega = \pm\beta\sqrt{(1-3\sigma')(1-\sigma')}$, so they are linearly stable for $0 < \sigma' \leq 1/3$ and unstable for $1/3 < \sigma' < 1$.

(II) Mixed-mode dipoles: $\omega = \pm 2\beta\frac{\sqrt{2\sigma'(3\sigma'-1)}}{1+3\sigma'}$, so they are linearly stable for $1/3 \leq \sigma' < 1$ and unstable for $0 < \sigma' < 1/3$.

(III) Vortices: $\omega = \pm 2\beta\frac{\sqrt{2\sigma'(1-\sigma')}}{1+\sigma'}$, so they are always linearly stable for $0 < \sigma' < 1$.

IV. SQUARE LATTICE

In a square lattice and for symmetric potential $V(x,y) = V(y,x)$, taking into account nearest-neighbor (NN) and next-nearest-neighbor (NNN) (diagonal) couplings only between individual dipole modes, the general Eqs. (2) take the form

$$i\frac{dA_{m,j}}{dz} + C_1(A_{m+1,j} + A_{m-1,j}) - C_2(A_{m,j+1} + A_{m,j-1})$$
$$- C^{AA}(A_{m+1,j+1} + A_{m+1,j-1} + A_{m-1,j+1} + A_{m-1,j-1})$$
$$+ C^{AB}(B_{m+1,j+1} - B_{m+1,j-1} - B_{m-1,j+1} + B_{m-1,j-1})$$
$$+ \gamma|A_{m,j}|^2 A_{m,j} + \sigma(2|B_{m,j}|^2 A_{m,j} + B_{m,j}^2 A_{m,j}^*) = 0,$$

$$i\frac{dB_{m,j}}{dz} - C_2(B_{m+1,j} + B_{m-1,j}) + C_1(B_{m,j+1} + B_{m,j-1})$$
$$- C^{AA}(B_{m+1,j+1} + B_{m+1,j-1} + B_{m-1,j+1} + B_{m-1,j-1})$$
$$+ C^{AB}(A_{m+1,j+1} - A_{m+1,j-1} - A_{m-1,j+1} + A_{m-1,j-1})$$
$$+ \gamma|B_{m,j}|^2 B_{m,j} + \sigma(2|A_{m,j}|^2 B_{m,j} + A_{m,j}^2 B_{m,j}^*) = 0. \quad (3)$$

We illustrate the dipole coupling in a square lattice geometry in Fig. 2. Here, the lattice is defined by $(x,y) = (ja, ma)$, where a is the lattice constant [notice that the meaning of indices j and m is different than in Eq. (2)]. Note, as a consequence of the dipolelike nature of the couplings, the special way in which the individual coupling terms appear in Eq. (3) and in particular their signs. We have chosen the signs so that all coupling constants C_1, C_2, C^{AA}, C^{AB} will be positive in the physically relevant situations. Although the
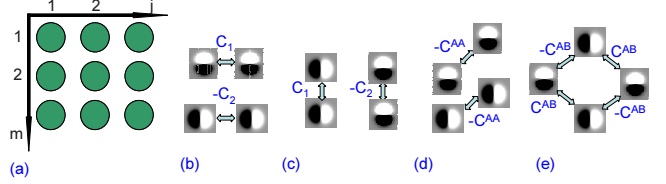

FIG. 2. (Color online) Schematic illustration of (a) a square lattice and coupling between dipole modes. [(b) and (c)] Horizontal and vertical C_1, C_2. (d) Diagonal between the modes of the same symmetry C^{AA}. (e) Diagonal between dipoles of different symmetries C^{AB}.

NNN coupling constants C^{AA} (self-coupling) and C^{AB} (cross-coupling) will generally be different, we may assume them to be of the same order of magnitude and typically some order of magnitude smaller than the NN coupling constants C_1 and C_2, since the individual waveguide modes are assumed to be exponentially decaying with the waveguide separation. Note also, $C_1 \neq C_2$ generally, so that anisotropy appears in each of the two equations in Eq. (3) due to the anisotropy of the dipole waveguide modes, although the full system is isotropic.

The two conserved quantities for Eqs. (3) are the Hamiltonian

$$H = \sum_{m,j}\left\{ 2C_1\text{Re}(A_{m,j}A_{m+1,j}^* + B_{m,j}B_{m,j+1}^*) - 2C_2\text{Re}(A_{m,j}A_{m,j+1}^* \right.$$
$$+ B_{m,j}B_{m+1,j}^*) - 2C^{AA}\text{Re}[A_{m,j}(A_{m+1,j+1}^* + A_{m+1,j-1}^*)$$
$$+ B_{m,j}(B_{m+1,j+1}^* + B_{m+1,j-1}^*)] + 2C^{AB}\text{Re}[A_{m,j}(B_{m+1,j+1}^*$$
$$- B_{m+1,j-1}^*) + B_{m,j}(A_{m+1,j+1}^* - A_{m+1,j-1}^*)] + \frac{\gamma}{2}(|A_{m,j}|^4$$
$$\left. + |B_{m,j}|^4) + \sigma(2|A_{m,j}|^2|B_{m,j}|^2 + \text{Re}[A_{m,j}^2 B_{m,j}^{*2}]) \right\} \quad (4)$$

and the total power (norm)

$$P = \sum_{m,j}(|A_{m,j}|^2 + |B_{m,j}|^2). \quad (5)$$

It is also useful to express Eqs. (3) in terms of oppositely charged vortex modes ("circularly polarized modes," cf., e.g., [13])

$$U_{m,j} = \frac{1}{2}[(-1)^j A_{m,j} + i(-1)^m B_{m,j}],$$

$$V_{m,j} = \frac{1}{2}[(-1)^j A_{m,j} - i(-1)^m B_{m,j}],$$

where the staggering factors $(-1)^j$ and $(-1)^m$ are introduced due to the negative signs in front of C_2 in Eq. (3). Then, the equations of motion take the form

$$i\frac{dU_{m,j}}{dz} + \frac{C_1+C_2}{2}(U_{m+1,j} + U_{m-1,j} + U_{m,j+1} + U_{m,j-1})$$

$$+ \frac{C_1-C_2}{2}(V_{m+1,j} + V_{m-1,j} - V_{m,j+1} - V_{m,j-1})$$

$$+ C^{AA}(U_{m+1,j+1} + U_{m+1,j-1} + U_{m-1,j+1} + U_{m-1,j-1})$$

$$- (-1)^{m+j}iC^{AB}(V_{m+1,j+1} - V_{m+1,j-1} - V_{m-1,j+1} + V_{m-1,j-1})$$

$$+ (\gamma+\sigma)(|U_{m,j}|^2 + 2|V_{m,j}|^2)U_{m,j} + (\gamma-3\sigma)V_{m,j}^2 U_{m,j}^* = 0,$$

$$i\frac{dV_{m,j}}{dz} + \frac{C_1+C_2}{2}(V_{m+1,j} + V_{m-1,j} + V_{m,j+1} + V_{m,j-1})$$

$$+ \frac{C_1-C_2}{2}(U_{m+1,j} + U_{m-1,j} - U_{m,j+1} - U_{m,j-1})$$

$$+ C^{AA}(V_{m+1,j+1} + V_{m+1,j-1} + V_{m-1,j+1} + V_{m-1,j-1})$$

$$+ (-1)^{m+j}iC^{AB}(U_{m+1,j+1} - U_{m+1,j-1} - U_{m-1,j+1}$$

$$+ U_{m-1,j-1}) + (\gamma+\sigma)(|V_{m,j}|^2 + 2|U_{m,j}|^2)V_{m,j}$$

$$+ (\gamma-3\sigma)U_{m,j}^2 V_{m,j}^* = 0, \qquad (6)$$

the Hamiltonian

$$H' = \sum_{m,j}\Bigg\{ (C_1+C_2)\mathrm{Re}[U_{m,j}(U_{m+1,j}^* + U_{m,j+1}^*)$$

$$+ V_{m,j}(V_{m+1,j}^* + V_{m,j+1}^*)] + (C_1-C_2)\mathrm{Re}[U_{m,j}(V_{m+1,j}^*$$

$$+ V_{m-1,j}^* - V_{m,j+1}^* - V_{m,j-1}^*)] + 2C^{AA}\mathrm{Re}[U_{m,j}(U_{m+1,j+1}^*$$

$$+ U_{m+1,j-1}^*) + V_{m,j}(V_{m+1,j+1}^* + V_{m+1,j-1}^*)]$$

$$- 2C^{AB}(-1)^{m+j}\mathrm{Im}[U_{m,j}(V_{m+1,j+1}^* - V_{m+1,j-1}^* + V_{m-1,j+1}^*$$

$$- V_{m-1,j+1}^*)] + \frac{\gamma+\sigma}{2}(|U_{m,j}|^4 + |V_{m,j}|^4) + 2(\gamma+\sigma)$$

$$\times(|U_{m,j}|^2|V_{m,j}|^2 + (\gamma-3\sigma)\mathrm{Re}[U_{m,j}^2 V_{m,j}^{*2}])\Bigg\}, \qquad (7)$$

and the total power (norm)

$$P = \sum_{m,j}(|U_{m,j}|^2 + |V_{m,j}|^2). \qquad (8)$$

From this, it follows that in the special case when $\sigma'=1/3$ (circular waveguides), $C_1=C_2$ (isotropic NN mode coupling), and $C^{AB}=0$ (no NNN cross coupling between individual dipole modes), the two vortex fields $U_{m,j}$ and $V_{m,j}$ do not mix, so that we have independent conservation of the power of each field, $P_U=\Sigma_{m,j}|U_{m,j}|^2$, $P_V=\Sigma_{m,j}|V_{m,j}|^2$. However, in the general case, only total power (8) is conserved.

A. NN interactions

We first consider the case where the NNN interactions can be neglected and thus put $C^{AA}=C^{AB}=0$ in Eq. (3). In this case, it is enough to consider, e.g., $\gamma>0$, since changing the sign of γ is mathematically equivalent to a staggering transformation combined with $z\to-z$. We should also remark that in the limit case of $\sigma=0$ (uncoupled horizontal and vertical

modes), the model turns into two uncoupled simple discrete nonlinear Schrödinger (DNLS) equations with anisotropic dispersion, which has been analyzed, e.g., in [14,15].

Let us first discuss the linear dispersion relation for the NN case. Putting

$$A_{m,j} = A_0\exp[i(\kappa_1^{(A)}j + \kappa_2^{(A)}m)]\exp(i\beta^{(A)}z),$$

$$B_{m,j} = B_0\exp[i(\kappa_1^{(B)}j + \kappa_2^{(B)}m)]\exp(i\beta^{(B)}z),$$

with $|A_0|,|B_0|\ll1$, and inserting into Eqs. (3) with $C^{AA}=C^{AB}=\gamma=\sigma=0$, we arrive at the dispersion relation for the two uncoupled fields in the small-amplitude limit

$$\beta^{(A)} = 2C_1\cos\kappa_2^{(A)} - 2C_2\cos\kappa_1^{(A)} \equiv \beta^{(A)}(\kappa_1^{(A)},\kappa_2^{(A)}),$$

$$\beta^{(B)} = 2C_1\cos\kappa_1^{(B)} - 2C_2\cos\kappa_2^{(B)} \equiv \beta^{(B)}(\kappa_1^{(B)},\kappa_2^{(B)}). \quad (9)$$

Note that, since $\beta^{(B)}(\kappa_1,\kappa_2)=\beta^{(A)}(\kappa_2,\kappa_1)$, the two linear bands associated with $A-$ and $B-$ modes completely overlap. The dispersion relation has its maximum for $\kappa_2^{(A)}=\kappa_1^{(B)}=0$, $\kappa_1^{(A)}=\kappa_2^{(B)}=\pi$, and thus solitons are expected to bifurcate from the corresponding band edge at $\beta=2(C_1+C_2)$ when the soliton amplitude goes to zero.

Similarly as in, e.g., [12] and references therein, we may use the three types I, II, and III of stationary solutions for an isolated waveguide in Sec. III as "anticontinuous" limits $(C_1\to0, C_2\to0)$ for solutions of the full lattice and as is well known, such solutions are expected to persist for finite coupling under quite general conditions. Explicitly, they may be numerically calculated using standard Newton-type schemes and moreover approximate analytical expressions may be obtained, e.g., through perturbation expansions using the coupling constants as small parameters. In this paper, we give a complete classification of the existence and stability properties of the *fundamental* stationary states, obtained as continuations of anticontinuous solutions with only one single waveguide excited. As we shall see, all these solutions may be smoothly continued, for increasing coupling, all the way to the continuum limit, where the solutions approach standard vector solitons with well-known envelopes (see, e.g., [9] and references therein and recent papers [7,8]). In addition, one may also consider composite states consisting of, e.g., multiple vortices with different positions and charges or dipoles with different orientations at different lattice sites at the anticontinuous limit, as well as nonstationary solutions (e.g., with periodic power exchange between fields A and B); however, these issues will be left for future investigations.

For convenience for the reader, we now wish to relate our classification of fundamental solutions to the terminology of other works.

(I) Our single (horizontal or vertical) dipole modes correspond to the "X solitary wave" of [1,2] (Figs. 10 and 11 in [2]), the "reduced-symmetry gap soliton" of [3], the "single-Bloch-mode soliton" of [7] [Figs. 5, 11(a), and 11(b) in [7]], and the "ellipsoidal positive soliton" of [8] [Fig. 7(c) in [8]].

(II) Our mixed (diagonal) dipole modes correspond to the "dipole-array gap soliton" of [7] [Figs. 6(c), 6(d), 11(c), 11(d), and 11(e) in [7]] and the "symmetric real coupled soliton" of [8] (Fig. 11 in [8]).

(III) Our vortex modes correspond to the "second-band vortex soliton" of [5,6], the "vortex-array gap soliton" of [7] [Figs. 6(e), 6(f), and 11(f)-11(h) in [7]), and the "$\pi/2$-phase delay coupled soliton" of [8] (Fig. 12 in [8]).

The linear stability analysis for a lattice of N sites now becomes equivalent to diagonalizing a $4N \times 4N$ matrix (cf. [10,12]), which at the anticontinuous limit has four eigenvalues corresponding to the eigenfrequencies for the single-excited waveguide given in Sec. III and the remaining eigenfrequencies, corresponding to the $N-1$ unexcited waveguides, located as $2(N-1)$ pairs of eigenfrequencies $\omega = \pm \beta$.

1. $\sigma' \neq 1/3$.

Let us first discuss the case $\sigma' \neq 1/3$ (noncircular waveguides), for which the situation is rather simple. The stability properties may be summarized as follows:

(i) Dipole modes (I, II) keep their stability properties from the anticontinuous limit (and in addition become unstable through the Vakhitov-Kolokolov (VK) "quasicollapse" instability close to continuum limit).

(ii) Vortex modes (III) are stable for weak coupling, but become oscillatorily unstable for larger coupling due to a resonance between localized internal-mode oscillations and extended modes from the linear band (see, e.g., [16] for a similar scenario).

The behaviors of the eigenvalues close to the anticontinuous limit have been obtained analytically to second order in the coupling constants by diagonalization (with help of Maple) of the 12×12 matrix corresponding to the excited site and two nearest neighbors in horizontal, respectively, vertical directions (using appropriate symmetry relations). For example, for the vortex modes III, we obtain

$$\omega = \pm 2\beta \frac{\sqrt{2\sigma'(1-\sigma')}}{1+\sigma'} \left[1 - \frac{2(C_1^2 + C_2^2)}{\beta^2} \right] + O(C^4).$$

Equating this to the expression for the edge of the linear band, $\omega = \beta - 2(C_1 + C_2)$, and solving, e.g., for C_1/β gives an estimate for the instability threshold as a function of the other parameters C_2/β and σ'.

2. $\sigma' = 1/3$.

For $\sigma' = 1/3$ (circular waveguides), the situation is more intricate due to the additional degeneracy at the anticontinuous limit. First, in the special (isotropic) case $C_1 = C_2$, the degeneracy persists and the dipole modes remain marginally stable for all values of the coupling constant (except close to the continuum limit, where quasicollapse instabilities always appear).

However, as soon as $C_1 \neq C_2$, the degeneracy is broken and we find that the solutions continued from the single-mode (horizontal or vertical) dipoles (I) are stable, while those continued from the mixed-mode (diagonal) dipoles (II) are unstable. Thus, we recover the physically reasonable result that the favorable orientation of the individual dipoles is selected by the lattice directions (cf. experimental and numerical results in [3]). In both cases, the additional eigenvalue pair is found to bifurcate from $\omega = 0$ to order C_1^2, C_2^2

along the real, respectively, imaginary axis. However, in this case, it is nontrivial to obtain the correct lowest-order behavior analytically due to the fourfold degeneracy of the eigenvalue $\omega = 0$ at the anticontinuous limit. This would necessitate taking into account not only three but six main nonequivalent sites (central site, one nearest and one next-nearest neighbor in a horizontal and a vertical direction, respectively, and one diagonal site), leading to the rather formidable task of diagonalizing a 24×24 matrix.

For vortex modes (III), we first note that the nonzero eigenvalue pair at the anticontinuous limit is located at $\omega = \pm \beta$, i.e., degenerate with the frequency of linear oscillations for the remaining unexcited sites. As the coupling is increased, this eigenvalue bifurcates from $\omega = \pm \beta$, again to order $C_1^2 + C_2^2$ and therefore the real part of this eigenvalue remains inside the band of linear oscillations ($|\omega| \in [\beta - 2(C_1 + C_2), \beta + 2(C_1 + C_2)]$), where it causes oscillatory instabilities (complex eigenvalues) colliding with extended linear eigenmodes. Thus, strictly speaking, the vortex mode is always unstable for $\sigma' = 1/3$ for infinite lattices (when the linear band is continuous), but for small C, the instabilities are very weak and practically invisible and moreover for a finite system they appear only in narrow windows due to the discrete nature of the linear "band" (cf. [16] and references therein). This behavior is illustrated in Fig. 3. An exception to this behavior, which is generic for $C_2 \neq C_1$, appears in the isotropic case $C_2 = C_1$. In this case, even though the localized mode exists inside the linear spectrum just as in Fig. 3, no resonances appear and the vortex mode remains linearly stable until the quasicollapse regime appears close to the continuum limit. This is a consequence of the dispersive decoupling of the two vortex fields U and V in Eq. (6). Due to this, also the corresponding linearized equations decouple when $C_1 = C_2$ and $V \equiv 0$ (or $U \equiv 0$), so that eigenmodes belonging to different subspectra do not interact. But as soon as $C_2 \neq C_1$, they interact through the dispersive coupling terms and instabilities should develop.

B. Effect of NNN interactions

In the case of NNN interactions, to give a complete characterization we must consider independently both signs of nonlinearity $\gamma = \pm 1$. However, it is still enough to consider, e.g., $C_2 \leq C_1$, since the transformation $A'_{m,j} = (-1)^{m+j} B_{m,j}, B'_{m,j} = (-1)^{m+j} A_{m,j}$ switches the roles of C_2 and C_1.

Our extensive numerical investigations may be summarized as follows:

(i) A sufficiently weak NNN interaction does not change the stability properties of the NN case, except when stability is marginal in absence of NNN.

(ii) For stronger NNN interactions, there may be stability inversions between the two different types of dipole modes so that for $\sigma' = 1/3$, the mixed-mode (type II) dipoles (oriented in the diagonal directions) become stable and the single-mode (type I) dipoles (oriented in the lattice directions) become unstable. Again, this is physically reasonable, since strong NNN (diagonal) interactions should favor alignment in diagonal directions. This behavior is illustrated in Fig. 4.
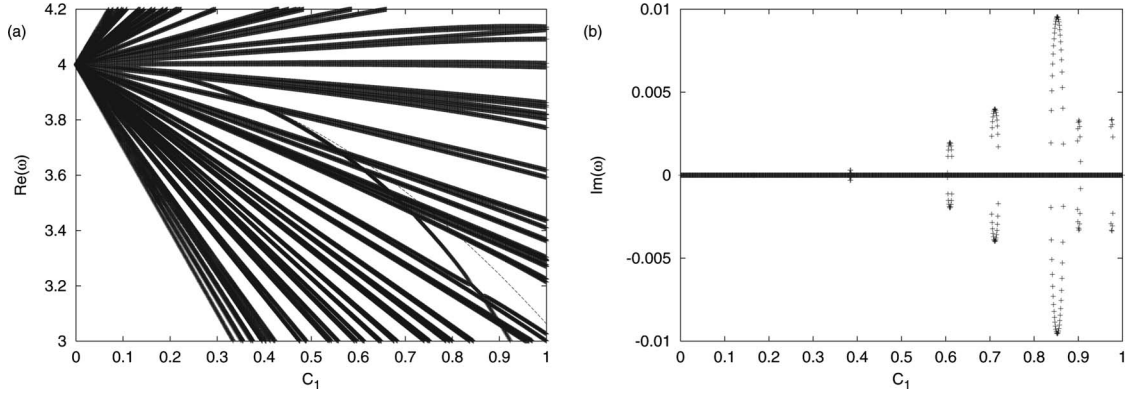
FIG. 3. (a) Real and (b) imaginary parts of eigenfrequencies of linear oscillations for a fundamental vortex (type III) stationary solutions in a square lattice described by Eq. (3) with $\gamma=1$ and $\sigma=1/3$ as a function of coupling constant C_1 with $C_2=C_1/2$, pure NN interactions ($C^{AA}=C^{AB}=0$), $\beta=4$, and system size 11×11 sites. In (a), the linearly spreading eigenfrequencies represent extended eigenmodes (constituting the continuous linear band when the system size becomes infinite), while the eigenfrequency with quadratic behavior corresponds to the localized internal mode, whose frequency for weak coupling can be approximated as $\mathrm{Re}(\omega)=\beta-3(C_1^2+C_2^2)/\beta$ [dashed line in (a)]. (b) illustrates windows of instability [nonzero $\mathrm{Im}(\omega)$] which become dense as the system size becomes infinite.

(iii) When the anisotropy becomes weak (C_2 close to C_1), the strength of NNN interaction needed to invert stability for $\sigma'=1/3$ decreases. For example, with $C_2=0.9C_1$ and $C^{AA}=C^{AB}=0.15C_1$, stability is inverted and diagonal (type II) dipole modes stable for $0.09\lesssim C_1/\beta\lesssim0.18$ (the latter value corresponding to VK instability) when $\gamma=+1$.

(iv) In particular, in the isotropic case $C_2=C_1$ where both types of dipole modes are marginally stable for $\sigma'=1/3$ in absence of NNN interactions, any arbitrary nonzero value of C^{AB} breaks the marginal stability and makes diagonal (type II) modes stable and horizontal or vertical (type I) modes unstable. Note however that this is an effect of the anisotropic nature of the cross-coupling C^{AB}; if $C^{AB}=0$, marginal stability survives for all values of the isotropic NNN-coupling C^{AA}.

(v) Also for vortex (type III) modes, inclusion of the NNN cross couplings breaks the marginal stability at $C_1=C_2$ and causes weak oscillatory instabilities via phonon resonances. This happens since the linearized equations corresponding to Eqs. (6) are no more decoupled even though one of the fields U or V is zero, since they get coupled by the C^{AB} terms.

(vi) For $\gamma=-1$, the main qualitative conclusions are the same as for $\gamma=+1$. However, the quantitative behavior is somewhat more intricate, particularly for weak anisotropy where multiple exchanges of stability between type-I and type-II dipole modes may appear as illustrated in Fig. 5.

V. TRIANGULAR LATTICE

For describing a triangular lattice, we take into account only the NN couplings between horizontal and vertical di-
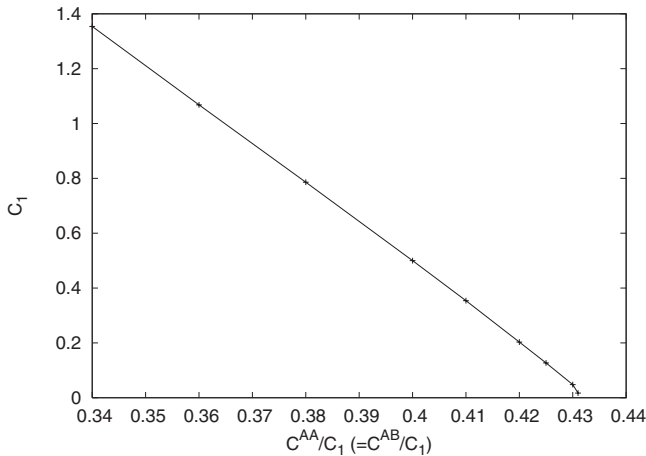

FIG. 4. Stability threshold for dipole modes in square lattice (3) with NNN interactions $C^{AA}=C^{AB}$ and NN anisotropy $C_2/C_1=1/2$, for $\sigma=1/3$, $\gamma=+1$, and $\beta=8$. Type-I (horizontal/vertical) dipole modes are stable below the line, while type-II (diagonal) dipole modes are stable above. For $C^{AA}/C_1=C^{AB}/C_1\gtrsim0.431$, type-I dipoles are always unstable. In addition, quasicollapse (VK) instabilities appear for $C_1\gtrsim1.4$ so that type II dipoles are always unstable for $C^{AA}/C_1=C^{AB}/C_1\lesssim0.33$.
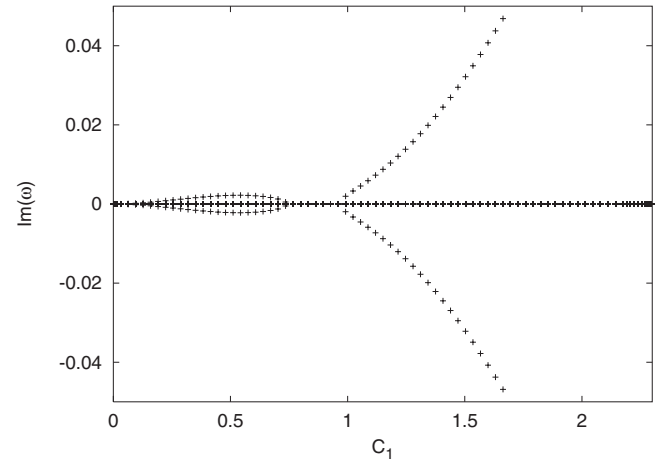

FIG. 5. Unstable eigenvalue for type-I dipole modes in square lattice (3) with NNN interactions $C^{AA}=C^{AB}=0.2$ and NN anisotropy $C_2/C_1=0.99$ for $\sigma'=1/3$, $\gamma=-1$, and $|\beta|=8$. Note the stable window for $0.75\lesssim C_1\lesssim0.95$, where the otherwise stable (diagonal) type-II mode instead becomes unstable. In addition, quasicollapse (VK) instabilities appear for both modes for $C_1\gtrsim2.1$. The latter is considerably stronger, with max. $\mathrm{Im}(\omega)\simeq1.5$ for $C_1\simeq2.3$, and therefore not visible on the scale of this figure.
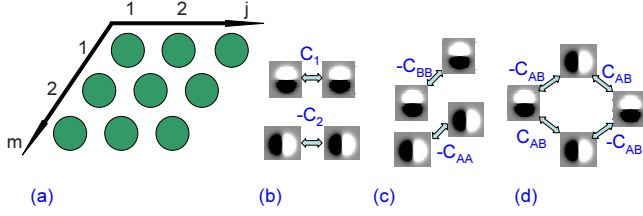
FIG. 6. (Color online) Schematic illustration of (a) a triangular lattice and coupling between dipole modes. (b) Horizontal (C_1 and C_2). (c) Diagonal between the modes of the same symmetry (C_{AA} and C_{BB}). (d) Diagonal between dipoles of different symmetries C_{AB}.

pole modes localized at a given waveguide with the corresponding dipole modes localized at its six nearest neighbors. (We remark that for the simple DNLS model on an isotropic triangular lattice, also effects of long-range interactions have been considered in [17].) We define lattice indices as

$$(x,y) = [(j - m/2)a, m\sqrt{3}a/2], \qquad (10)$$

where a is the lattice constant [notice again that the meaning of indices j and m is different than in Eq. (2)]. In other words, one lattice direction is assumed to be horizontal and described by the index j, while the index m describes the translation in a lattice direction rotated 60° with respect to the horizontal. Then, as a consequence of the dipolelike nature of the couplings, the general Eqs. (2) take the form

$$i\frac{dA_{m,j}}{dz} - C_2(A_{m,j+1} + A_{m,j-1}) - C_{AA}(A_{m+1,j} + A_{m-1,j} + A_{m+1,j+1}$$
$$+ A_{m-1,j-1}) - C_{AB}(B_{m+1,j} + B_{m-1,j} - B_{m+1,j+1} - B_{m-1,j-1})$$
$$+ \gamma|A_{m,j}|^2 A_{m,j} + \sigma(2|B_{m,j}|^2 A_{m,j} + B_{m,j}^2 A_{m,j}^*) = 0,$$

$$i\frac{dB_{m,j}}{dz} + C_1(B_{m,j+1} + B_{m,j-1}) - C_{BB}(B_{m+1,j} + B_{m-1,j} + B_{m+1,j+1}$$
$$+ B_{m-1,j-1}) - C_{AB}(A_{m+1,j} + A_{m-1,j} - A_{m+1,j+1} - A_{m-1,j-1})$$
$$+ \gamma|B_{m,j}|^2 B_{m,j} + \sigma(2|A_{m,j}|^2 B_{m,j} + A_{m,j}^2 B_{m,j}^*) = 0. \qquad (11)$$

Here, as before we have chosen the signs so that the self-coupling constants C_1, C_2 in the horizontal lattice direction between vertically, respectively, horizontally oriented dipoles are always positive. In addition, the signs have been chosen so that also the cross-coupling constant C_{AB} generally is positive, while the self-coupling coefficients C_{AA}, C_{BB} in the other directions may be either positive or negative depending on the particular geometry of the waveguides and the shape of the potential $V(x,y)$ in the physical realization. Thus, for the most general case, we now have five independent coupling constants (with the above-mentioned sign restrictions) and the self-coupling and cross-coupling constants will generally all be of the same order of magnitude. We illustrate the dipole coupling in a triangular lattice geometry in Fig. 6.

The Hamiltonian for the triangular lattice is

$$H = \sum_{m,j} \left\{ 2C_1\mathrm{Re}(B_{m,j}B_{m,j+1}^*) - 2C_2\mathrm{Re}(A_{m,j}A_{m,j+1}^*) \right.$$
$$- 2C_{AA}\mathrm{Re}[A_{m,j}(A_{m+1,j}^* + A_{m+1,j+1}^*)] - 2C_{BB}\mathrm{Re}[B_{m,j}(B_{m+1,j}^*$$
$$+ B_{m+1,j+1}^*)] + 2C_{AB}\mathrm{Re}[A_{m,j}(B_{m+1,j+1}^* - B_{m+1,j}^*)$$
$$+ B_{m,j}(A_{m+1,j+1}^* - A_{m+1,j}^*)] + \frac{\gamma}{2}(|A_{m,j}|^4 + |B_{m,j}|^4)$$
$$\left. + \sigma(2|A_{m,j}|^2|B_{m,j}|^2 + \mathrm{Re}[A_{m,j}^2 B_{m,j}^{*2}]) \right\}. \qquad (12)$$

We will here concentrate on the case of circular symmetric waveguides ($\sigma' = 1/3$) and leave a more complete discussion on effects which may occur if the symmetry of a single (noncircular) waveguide (e.g., square) differs from the symmetry of the triangular lattice to future investigations. Then, for cylindrical waveguides [or, more generally, for waveguides having the same (sixfold) rotational symmetry as the lattice (or higher)], the following relations between the coupling constants follow by straightforward geometrical arguments from the transformation of the waveguide modes Ψ_a and Ψ_b under $\pi/3$ rotations

$$C_{AA} = \frac{1}{4}(C_2 - 3C_1),$$

$$C_{AB} = \frac{\sqrt{3}}{4}(C_2 + C_1),$$

$$C_{BB} = \frac{1}{4}(3C_2 - C_1). \qquad (13)$$

Thus, we see that, while $C_{AB} > 0$ always, $C_{AA} > 0$ only if $C_2 > 3C_1$, while $C_{BB} > 0$ only if $C_2 > C_1/3$. [We remark that if $C_1 = 0$, the relations (13) for the linear coupling coefficients become equivalent to those considered in a model for longitudinal and transverse waves in two-dimensional hexagonal dusty plasma crystals [18–21].]

Then, due to the sixfold rotational symmetry of the lattice+waveguides, three classes of distinct fundamental stationary solutions appear from the anticontinuous limit:

(i) "Horizontal" dipole modes: $A_{m_0,j_0} = \pm\sqrt{\beta/\gamma}\exp(i\beta z)$; $B_{m_0,j_0} = 0$. Equivalent solutions pointing in the other lattice directions, i.e., rotated $n \cdot 60°$, are obtained for $B_{m_0,j_0} = \pm\sqrt{3}A_{m_0,j_0}$.

(ii) "Vertical" dipole modes: $A_{m_0,j_0} = 0$; $B_{m_0,j_0} = \pm\sqrt{\beta/\gamma}\exp(i\beta z)$. Equivalent solutions, rotated $n \cdot 60°$, are obtained for $B_{m_0,j_0} = \pm\frac{1}{\sqrt{3}}A_{m_0,j_0}$. (Note that vertical dipole modes are distinct from horizontal for the triangular lattice, since their dipole moment points in-between two lattice directions.)

(iii) Vortex modes: $B_{m_0,j_0} = \mp iA_{m_0,j_0}$ (invariant under rotation, except for an overall phase change).

We also note that generally, Eqs. (11) are invariant under the following transformation (corresponding to 90° rotation):

$$A_{m,j} \to B_{m,j}, B_{m,j} \to -A_{m,j}, \gamma \to -\gamma, \sigma \to -\sigma, z \to -z,$$
$$C_1 \leftrightarrow C_2, C_{AA} \leftrightarrow -C_{BB}.$$

Therefore, for the special parameter relations defined by Eq. (13), we may either restrict our investigations to, e.g., $C_2 \leq C_1$ and $\gamma = \pm 1$ or to, e.g., $\gamma = +1$ and no restriction on C_2. We choose the first alternative.

Let us also discuss the linear dispersion relation for the triangular lattice with the parameter restrictions (13), which can be calculated in an analogous way as for the model in [18–21]. Using Eq. (10) (putting $a=1$), we express a lattice wave propagating in an arbitrary (transverse) direction in terms of the Cartesian physical components of its wave vector (κ_x, κ_y) as

$$A_{m,j} = A_0 \exp[i\kappa_x x + i\kappa_y y]\exp(i\beta z)$$
$$= A_0 \exp\left[i\kappa_x j - i\left(\frac{\kappa_x}{2} - \frac{\kappa_y\sqrt{3}}{2} \right)m + i\beta z \right],$$

$$B_{m,j} = B_0 \exp[i\kappa_x x + i\kappa_y y]\exp(i\beta z)$$
$$= B_0 \exp\left[i\kappa_x j - i\left(\frac{\kappa_x}{2} - \frac{\kappa_y\sqrt{3}}{2} \right)m + i\beta z \right],$$

with $|A_0|, |B_0| \ll 1$. Defining the propagation angle θ and magnitude of the wave vector κ as $\kappa_x = \kappa \cos\theta$, $\kappa_y = \kappa \sin\theta$, and inserting into Eqs. (11) with $\gamma = \sigma = 0$, we obtain two linear dispersion bands for the (in general) coupled A and B fields, which may be written in the form

$$\beta^{\pm}(\kappa, \theta) = (C_1 - C_2)\left\{ \cos[\kappa \cos\theta] + \cos\left[\kappa \cos\left(\theta - \frac{\pi}{3} \right) \right] \right.$$
$$\left. + \cos\left[\kappa \cos\left(\theta + \frac{\pi}{3} \right) \right] \right\}$$
$$\pm \frac{C_1 + C_2}{\sqrt{2}}\left\{ \left(\cos[\kappa \cos\theta] \right.\right.$$
$$\left. - \cos\left[\kappa \cos\left(\theta - \frac{\pi}{3} \right) \right] \right)^2 + \left(\cos[\kappa \cos\theta] \right.$$
$$\left. - \cos\left[\kappa \cos\left(\theta + \frac{\pi}{3} \right) \right] \right)^2 + \left(\cos\left[\kappa \cos\left(\theta - \frac{\pi}{3} \right) \right] \right.$$
$$\left.\left. - \cos\left[\kappa \cos\left(\theta + \frac{\pi}{3} \right) \right] \right)^2 \right\}^{1/2}. \quad (14)$$

Note that, due to the symmetry properties of the dispersion relation (14), all its nontrivial extrema occur for waves propagating either in a lattice direction ($\theta = 0 + n\pi/3$) or in-between lattice directions ($\theta = \pi/2 + n\pi/3$). In fact, for the particular angles $\theta = 0$ and $\theta = \pi/2$, the equations for the A and B fields decouple and we obtain two separate dispersion relations $\beta^{(A)}$ and $\beta^{(B)}$ corresponding to pure A and B modes, respectively,

$$\beta^{(A)}(\kappa, \theta = 0) = -2C_2 \cos\kappa + (3C_1 - C_2)\cos\frac{\kappa}{2},$$

$$\beta^{(B)}(\kappa, \theta = 0) = 2C_1\cos\kappa + (C_1 - 3C_2)\cos\frac{\kappa}{2},$$

$$\beta^{(A)}(\kappa, \theta = \pi/2) = -2C_2 + (3C_1 - C_2)\cos\frac{\kappa\sqrt{3}}{2},$$

$$\beta^{(B)}(\kappa, \theta = \pi/2) = 2C_1 + (C_1 - 3C_2)\cos\frac{\kappa\sqrt{3}}{2}. \quad (15)$$

Thus, assuming $0 \leq C_2 \leq C_1$ as above, we may deduce from these relations that the global minimum of the dispersion relation is $\beta = -(3C_1 + C_2)$, obtained for a solution with dipoles pointing in a lattice direction, with constant phases in this direction and alternating phases in the orthogonal direction. The location of the global maximum depends on the value of C_2/C_1. For $0 \leq C_2/C_1 \leq 1/3$, the global maximum is $\beta = 3(C_1 - C_2)$ and appears for $\kappa = 0$ (i.e., wave with constant phase, independent on dipole orientation). For $1/3 \leq C_2/C_1 \leq 1$, the global maximum is instead at $\beta = C_1 + 3C_2$ and is obtained for a solution with dipoles oriented orthogonal to a lattice direction, with constant phases in this lattice direction and alternating phases in the orthogonal direction. These extrema define the band edges from which solitons are expected to bifurcate for defocusing and focusing nonlinearities, respectively, in the limit of zero amplitude.

A. $C_1 = C_2$

We first discuss the case of "isotropic" interactions $C_1 = C_2 \equiv C$. Note however that although in this case the magnitude of the coupling between individual dipoles is the same whether they are both oriented in the lattice direction (C_2), or both oriented perpendicular to the lattice direction (C_1), the couplings in the 60° directions will still be different and thus the two equations in Eq. (11) are not themselves isotropic. Indeed, from Eq. (13), we get $C_{BB} = -C_{AA} = C/2$, $C_{AB} = \frac{\sqrt{3}}{2}C$.

Then, we may summarize the results from our numerical investigations as follows:

(1) For $\gamma = +1$, vertical dipole modes [type (ii)] are stable and horizontal modes [type (i)] are unstable. (For $\gamma = -1$, the result is opposite due to the above-mentioned symmetry.) The instability is however extremely weak close to the anti-continuous limit, with eigenvalues bifurcating from zero as $\omega/\beta \sim (C/\beta)^{13/2}$. This very unusual behavior, which is illustrated in Fig. 7, has been confirmed numerically not to be dependent on boundary conditions (by studying system sizes ranging between 81 and 289 sites) or on the precision used in the numerical algorithm (by using quadruple precision FORTRAN allowing determination of stability eigenvalues to a precision $\sim 10^{-16}$).

(2) Vortex modes are always oscillatorily unstable (but very weakly for small C and only in narrow windows for small systems), similarly as for the square lattice with $\sigma' = 1/3$. We should remark that although a transformation into vortex fields U, V leading to an equation analogous to Eq. (6) can be made, the equations for U and V are dispersively coupled even when $C_1 = C_2$ and therefore oscillatory instabilities are always present.
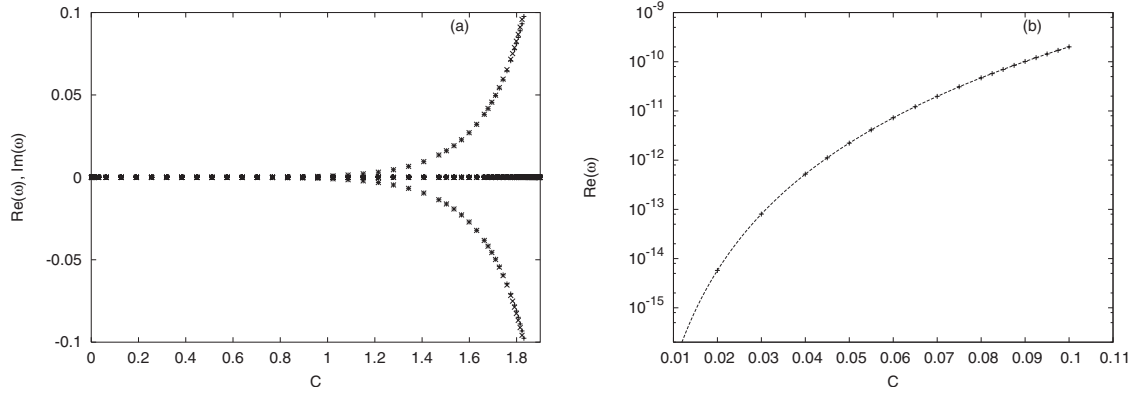
FIG. 7. (a) Simultaneous plot of $\text{Re}(\omega)$ for the stable vertical [type (ii)] ($\times$) and $\text{Im}(\omega)$ for the unstable horizontal [type (i)] (+) dipole modes in triangular lattice (11) with $C_1 = C_2 \equiv C$ and other coupling constants given by Eq. (13) for $\sigma' = 1/3$, $\gamma = +1$, and $\beta = 8$. Note that $\omega^{(i)} \simeq i\omega^{(ii)}$ for small C. In addition, quasicollapse (VK) instabilities appear for both modes for $C \gtrsim 1.7$. The latter is considerably stronger, with max. $\text{Im}(\omega) \simeq 1.3$ for $C \simeq 1.85$, and therefore not visible on the scale of this figure. (b) Logarithmic plot of the weak-coupling regime of (a) (points) together with the function $6.35 \times 10^{-4} C^{13/2}$ (dashed line).

(3) All modes can be continued toward the continuum limit, where VK ("quasicollapse") instabilities appear.

B. $C_2 \neq C_1$

For the general anisotropic case, when the magnitude of the interactions along lattice directions between horizontally pointed dipoles is different than between vertically pointed ($C_2 \neq C_1$), we summarize the main findings from our numerical investigations:

(1) For $C_2 < C_1$, vertical [type (ii)] modes are stable and horizontal [type (i)] modes unstable for both $\gamma = \pm 1$. (For $C_2 > C_1$, the result is opposite due to symmetry.) This is the physically expected result since vertical modes couple stronger in lattice directions when $C_1 > C_2$.

(2) The corresponding stability eigenvalues generally bifurcate from 0 as $\omega \sim (C_1^3, C_2^3)$ along the real, respectively, imaginary axis for the stable, respectively, unstable dipole mode.

(3) For most values of the anisotropy parameter C_2/C_1, the above stability properties are kept when increasing C_1 until the appearance of VK instabilities. However, for very weak anisotropy, a region of stability inversion appears before the VK unstable regime. For $C_2 < C_1$, this happens only for $\gamma = -1 (\gamma = +1$ for $C_2 > C_1$), where, e.g., for $C_2/C_1 = 0.95$, horizontal modes are stable and vertical modes unstable for $0.205 \lesssim C_1/\beta \lesssim 0.215$ (VK instabilities appear at the latter value). This can be related to the fact that for the isotropic case, horizontal modes are stable and vertical modes unstable when $\gamma = -1$ as discussed above.

(4) For vortex modes [type (iii)], the result is qualitatively the same as for $C_2 = C_1$.

Of particular interest is the fact that there are two sets of special parameter values (related by the above-mentioned symmetry transformation) with nongeneric behavior: $C_2 = C_1/3$ (implying $C_{BB} = 0$), $\gamma = +1$, and $C_2 = 3C_1$ (implying $C_{AA} = 0$), $\gamma = -1$. At these exceptional values, no VK instability is observed. Instead of approaching the unstable solution of the 2D NLS equation for large coupling, the solution approaches either a single one-dimensional linear (constant-

amplitude) band-edge mode in the strong-coupling direction (stable dipole mode), a superposition of two linear band-edge modes in the weak-coupling directions (unstable dipole mode), or a superposition of all three (vortex mode). As a consequence, the stable dipole-mode solution is expected to become mobile in one particular lattice direction, where it becomes broad and continuumlike. This is characterized by the appearance of a spatially antisymmetric localized internal mode in the eigenvalue spectrum, whose frequency approaches zero in the linear continuum limit. This behavior has been confirmed numerically for system sizes up to 29 $\times$ 29 and is illustrated in Fig. 8. On the other hand, although the VK instabilities disappear also for the vortex modes, they never gain mobility: no translational mode appears and their shape never becomes continuumlike since the amplitude of the central site is larger than that of the other sites in the linear superposition of three band-edge modes.

The above exceptional parameter values are the only cases where VK instabilities completely disappear (and, likewise, the only cases where the solitons bifurcate from linear modes with $P \to 0$, since generically there is always a power threshold for creation of solitons in 2D systems with cubic nonlinearity). However, for values close to these special values (e.g., $0.3 \lesssim C_2/C_1 \lesssim 0.4$), the regime of VK instability is very small and there are stable dipole-mode solutions with translational internal-mode frequency close to zero, which are expected also to show directional mobility. Examples are shown in Fig. 9.

VI. TRANSLATIONAL AND ROTATIONAL MOBILITIES OF DIPOLE MODES

Let us first briefly discuss the directional mobility of dipole modes in square lattices as observed in [3]. For brevity, we consider here Eq. (3) with only NN interactions ($C^{AA} = C^{AB} = 0$) and single-mode dipoles (I), which we know from Sec. IV A to be stable when $0 < \sigma' \leq 1/3$. With these restrictions, the study of mobility reduces to that of the one-component anisotropic DNLS since $B \equiv 0$ ($A \equiv 0$) for hori-
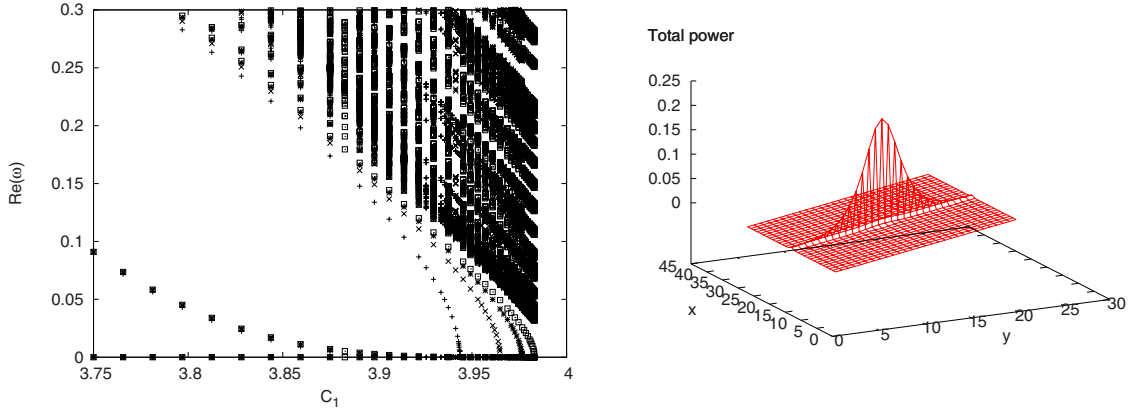
FIG. 8. (Color online) Left figure: Simultaneous plot of the spectrum of $\mathrm{Re}(\omega)$ for small ω and large coupling for the stable vertical [type (ii)] dipole mode in triangular lattice (11) with $C_2 = C_1/3$ and other coupling constants given by Eq. (13) for $\sigma' = 1/3$, $\gamma = +1$, and $\beta = 8$ for four different system sizes: $17 \times 17 (+)$, $21 \times 21 (\times)$, $25 \times 25 (*)$, and $29 \times 29 (\blacksquare)$. The isolated eigenvalue asymptotically approaching zero at the left part is the translational mode. Note that the bifurcation point at the right part of the figure approaches the value $C_1 = \beta/2$ as the system size increases, as expected for a one-dimensional band-edge mode. No VK instabilities appear for these parameter values. Right figure: Total power $|A_{m,j}|^2 + |B_{m,j}|^2$ for the solution with $C_1 = 3.95$ and system size 29×29.

zontal (vertical) dipole modes. This was studied in [15] and stable solutions mobile in the strong-coupling direction were found for $C_2/C_1 \lesssim 0.17$ [see Fig. 7(a) in [15]]. Similarly as for the triangular lattice with C_2/C_1 close to 1/3 illustrated in Figs. 8 and 9, we find that for $C_2/C_1 \lesssim 0.17$, a localized translational mode exists in the VK-stable regime and thus we should expect good directional mobility in this regime in agreement with [15].

A well-known approach to measure (translational) mobility of discrete modes [22] is to calculate the difference in energy (Hamiltonian) H at fixed power P between a "one-site" (centered at a lattice site) and a "two-site" (centered between lattice sites) mode. This so-called Peierls-Nabarro (PN) potential barrier then gives an estimate of the minimum energy needed to translate a stable mode along a lattice direction. As we are here also dealing with the possibility that dipole modes can be *rotated* in the lattice, we may analogously investigate their "rotational mobility" by defining a "rotational PN barrier" as the energy difference between stable and unstable dipole modes (at fixed power). This ro-

tational PN barrier should then describe the minimum additional energy needed for rotation of stable dipole modes.

To be specific, from now we consider only the particular case $\sigma' = 1/3$ (circular waveguides). We first in Fig. 10 show a comparison between translational and rotational PN barriers for a square lattice (NN interactions only) in a regime of reasonably good directional mobility ($C_2/C_1 = 0.15$). The structures of the modes used in determining the barriers are also shown in Fig. 10 for a value of the power where the rotational and translational PN barriers are approximately equal. The Hamiltonian and power of the modes are calculated using Eqs. (4) and (5) and the translational PN barrier is then calculated as the difference in H for each P between the stable one-site [Fig. 10(b)] and the unstable two-site [Fig. 10(c)] single-mode dipoles, while the rotational PN barrier is calculated as the difference in H for each P between the stable single-mode [Fig. 10(b)] and the unstable mixed-mode [Figs. 10(d) and 10(e)] one-site dipoles. (Note that the translational PN barrier here is calculated only in the "good-mobility" direction of strongest coupling and only for the
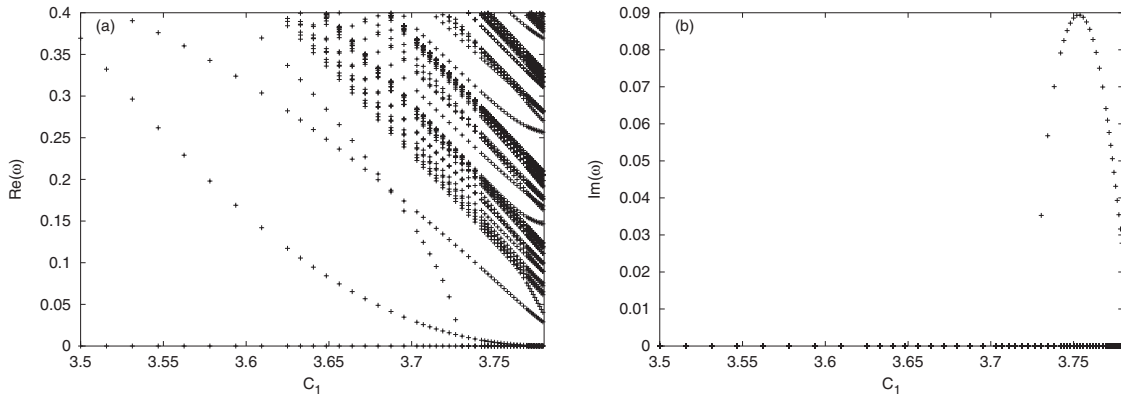

FIG. 9. (a) $\mathrm{Re}(\omega)$ for small ω and large coupling and (b) $\mathrm{Im}(\omega)$ for the stable vertical [type (ii)] dipole mode in triangular lattice (11) with $C_2 = 0.3 C_1$ and other coupling constants given by Eq. (13) for $\sigma' = 1/3$, $\gamma = +1$, and $\beta = 8$ and system size 21×21. The isolated eigenvalue asymptotically approaching zero at the lower left part of (a) is the translational mode and the eigenvalue colliding at 0 for $C_1 \simeq 3.73$ is the VK mode, yielding the instability shown in (b).
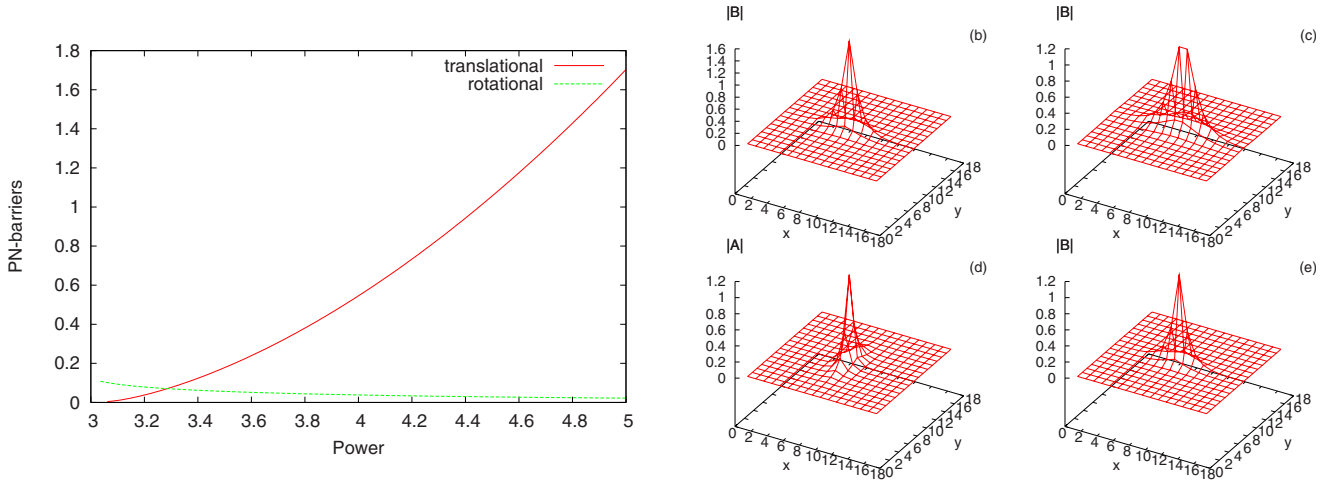
FIG. 10. (Color online) Left figure shows translational (solid red line) and rotational (dashed green line) PN barriers as a function of power for a square lattice with pure NN interactions $\sigma' = 1/3$, $C_2 = 0.15$, and $C_1 = 1$. Only VK-stable modes are included. Right figures show envelopes of the modes used to calculate the PN barriers at power $P \approx 3.28$ above. (b) Stable one-site vertical dipole mode ($A \equiv 0$). (c) Unstable two-site vertical dipole mode ($A \equiv 0$). [(d) and (e)] Unstable one-site mixed (diagonal) dipole mode.

rotationally stable single-mode state). As can be seen, the rotational PN barrier is monotonously decreasing toward zero for increasing power while the translational barrier is monotonously increasing and the curves intersect at a power $P \approx 3.28 C_1$.

The general pictures of translational and rotational PN barriers for different powers and anisotropy ratios C_2/C_1 are illustrated in Fig. 11. As can be seen, the general trends are that the translational PN barrier is increasing and the rotational PN barrier decreasing with increasing power. A more quantitative analysis of the decrease of the rotational PN barriers $\Delta H^{(rot)}$ shows an approximate power-law decay for large P, $\Delta H^{(rot)} \sim P^{-\mu}$, with $\mu \approx 2$ for all $0 < C_2/C_1 < 1$. This power-law decay at fixed C_1 and C_2 may be related to the power law of the bifurcation of the corresponding internal-mode eigenvalues from zero when increasing C_1 from zero at fixed β as discussed in Sec. IV A, $|\omega| \sim C_1^\nu$, with $\nu = 2$. Based on general scaling arguments, we may conjecture the relation $\mu = 2\nu - 2$ between the exponents (cf. results below for triangular lattice).

We should also note from Figs. 10 and 11 that the translational and rotational PN barriers may be of similar magnitudes only for strong anisotropy, $C_2/C_1 \lesssim 0.20$, and moderate

power $3 \lesssim P/C_1 \lesssim 3.5$. Note also the low-power cutoffs in the figures, illustrating the power thresholds which as expected decrease for increasing anisotropy as this means approaching a more one-dimensional situation. However, the power thresholds for the different solutions used in calculating the PN barriers are in general not identical and evidently the PN barriers are well-defined only for powers when both relevant solutions exist.

As a direct numerical illustration of the concepts of rotational PN barrier and rotational mobility, we show in Fig. 12 the evolution along z of the A and B parts of the central-site intensity, when a stable one-site vertical ($A \equiv 0$) dipole mode is given an initial perturbation at $z = 0$. As an example of a norm-conserving perturbation which may initiate rotation, we choose

$$A'_{m,j} = A_{m,j} \cos \epsilon + i B_{m,j} \sin \epsilon,$$

$$B'_{m,j} = B_{m,j} \cos \epsilon + i A_{m,j} \sin \epsilon. \tag{16}$$

As is seen from Fig. 12, the perturbed mode will begin to rotate if ϵ is larger than a threshold value. For these parameter values, the theoretically estimated rotational PN barrier
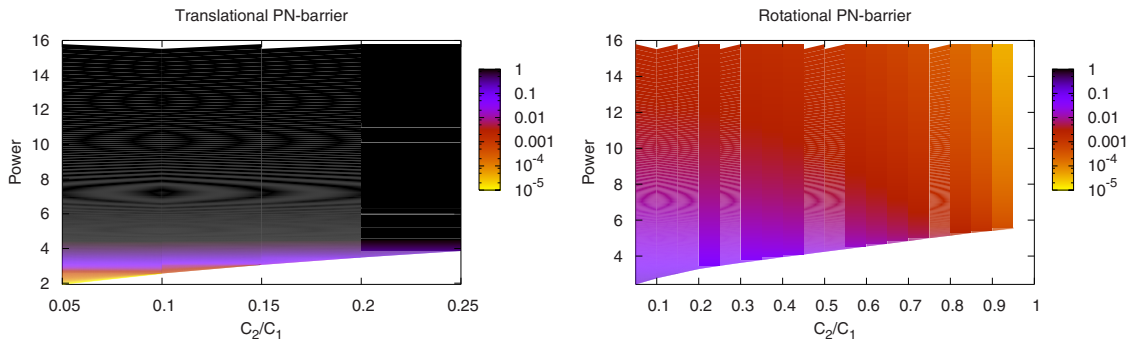

FIG. 11. (Color online) Translational (left figure) and rotational (right figure) PN barriers as a function of power and anisotropy ratio C_2/C_1 for a square lattice with pure NN interactions, $\sigma' = 1/3$ and $C_1 = 1$. Only VK-stable modes are included.
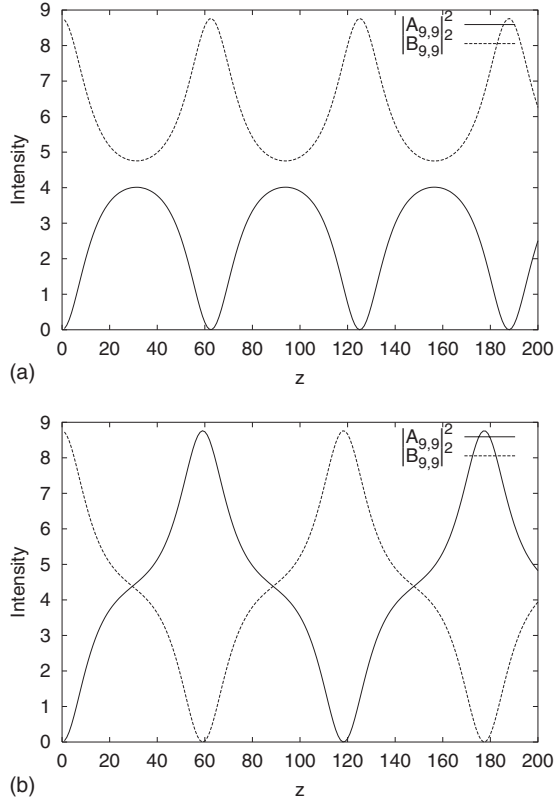
FIG. 12. Evolution along z for an initially perturbed stable one-site vertical dipole mode in a square lattice, with the same parameter values as in Fig. 10 but with $P=9$. Solid (dashed) lines show the A (B) parts of the central-site intensity. The perturbation is chosen from Eq. (16) with $\epsilon=0.0112$ (a) just below rotation threshold and $\epsilon=0.0113$ (b) just above rotation threshold. System size 17×17, periodic boundary conditions.

(cf. Fig. 11) is 6.1×10^{-3}, while the change of Hamiltonian for the threshold perturbation in Fig. 12(b) is 6.9×10^{-3}. This reflects the fact that a perturbation of the type (16) in general is not optimal and will excite several different eigenmodes. In this sense, the "best" perturbation should be along the exact eigenvector corresponding to the rotational eigenmode, but such a perturbation is probably more difficult to realize experimentally.

We then proceed to discuss the corresponding results for translational and rotational PN barriers for dipole modes in the triangular lattice. As discussed in Sec. V, we may still make the restriction to $C_2 \leq C_1$ without loss of generality, but then we have to treat the self-focusing and self-defocusing cases $\gamma = \pm 1$ separately. We first consider $\gamma=+1$, which is the only case where there is a regime of good translational directional mobility of stable dipole modes for $C_2 \leq C_1$ (see Sec. V B). Figure 13 shows a comparison between translational and rotational PN barriers for a triagonal lattice in a regime of reasonably good directional mobility ($C_2/C_1 =0.35$). The structures of the modes used in determining the barriers are also shown in Fig. 13 for a value of the power where the rotational and translational PN barriers are approximately equal. Analogously to the square lattice, the Hamiltonian and power of the modes are calculated using Eqs. (12) and (5) and the translational PN barrier is calculated as the difference in H for each P between the stable one-site [Figs. 13(b) and 13(c)] and the unstable two-site [Figs. 13(d) and 13(e)] vertical dipole modes, while the rotational PN barrier is calculated as the difference in H for each P between the stable vertical [Figs. 13(b) and 13(c)] and the unstable horizontal [Figs. 13(f) and 13(g)] one-site dipole modes. (Remember from Sec. V that all modes with dipoles pointing in lattice directions are equivalent to horizontal modes, while all modes with dipoles pointing between lattice directions are equivalent to vertical modes.)

As can be seen from Fig. 13, for these parameter values, the rotational PN barrier is monotonously decreasing toward
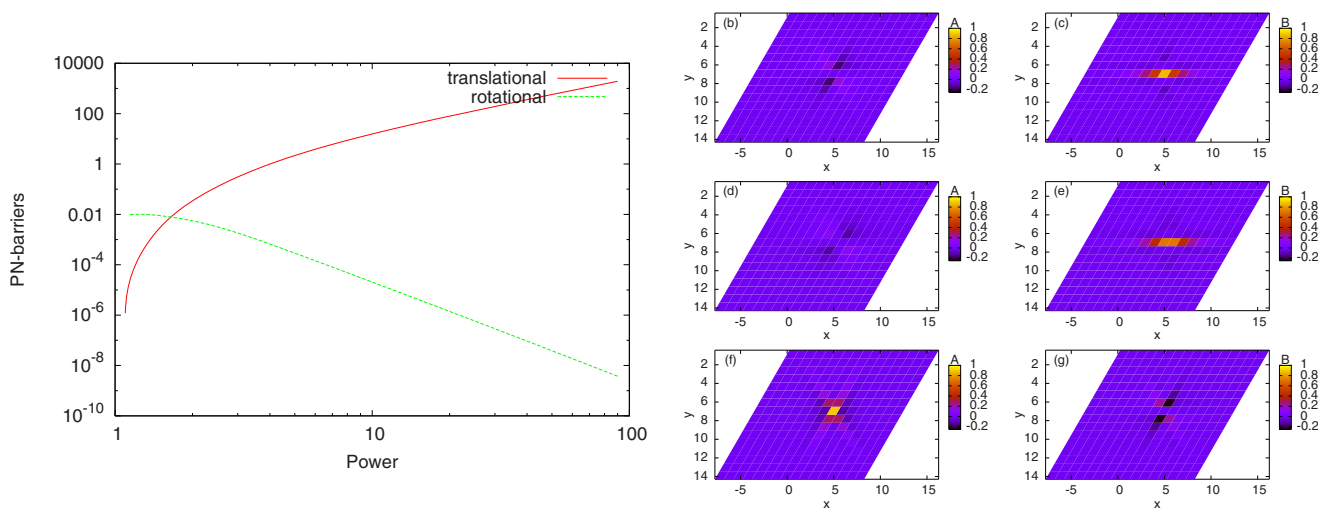

FIG. 13. (Color online) Left figure shows translational (solid red line) and rotational (dashed green line) PN barriers as a function of power for a triagonal lattice with $\gamma=+1$, $\sigma'=1/3$, $C_2=0.35$, $C_1=1$, and other coupling constants given by Eq. (13). Only VK-stable modes are included. Right figures show A and B components of the modes used to calculate the PN barriers at power $P \approx 1.65$. [(b) and (c)] Stable one-site vertical dipole mode. [(d) and (e)] Unstable two-site vertical dipole mode. [(f) and (g)] Unstable one-site horizontal dipole mode.
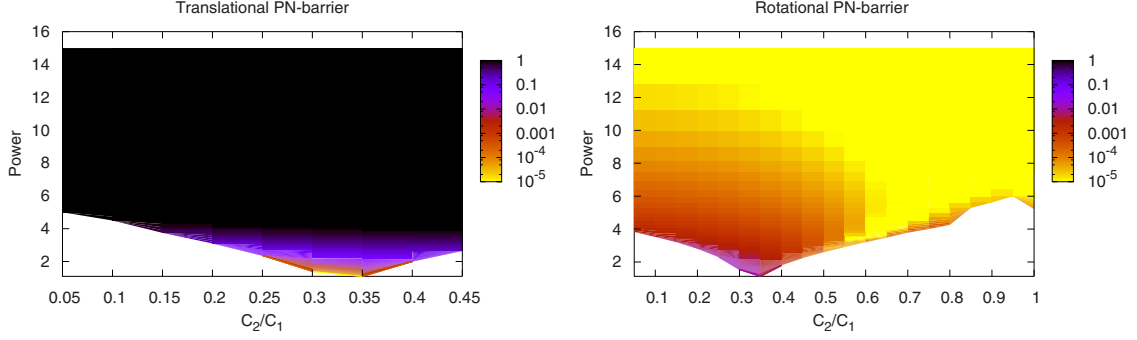
FIG. 14. (Color online) Translational (left figure) and rotational (right figure) PN barriers as a function of power and anisotropy ratio C_2/C_1 for a triangular lattice with $\gamma=+1$, $\sigma'=1/3$, $C_1=1$, and other coupling constants given by Eq. (13). Only VK-stable modes are included.

zero for increasing power while the translational barrier is monotonously increasing, just as for the square lattice, and the curves intersect at a power $P \approx 1.65 C_1$. However, a systematic study of the PN barriers for different anisotropy ratios C_2/C_1, summarized in Fig. 14, reveals a more complicated power dependence for the rotational barrier. For $0.5 \lesssim C_2/C_1 < 1$, the rotational PN barrier has a local (nonzero) minimum as well as a local maximum at some intermediate power levels. As for the square lattice, the decrease of the rotational PN barriers for large power at fixed C_1 and C_2 shows an approximate power-law decay $\Delta H^{(rot)} \sim P^{-\mu}$ (cf. the logarithmic plot in Fig. 13). Here, $\mu \approx 4$ for $0 < C_2/C_1 < 1$, consistent with the above-mentioned conjecture $\mu = 2\nu - 2$ since the corresponding internal-mode eigenvalues were found in Sec. V B to bifurcate from zero at fixed β as $|\omega| \sim C_1^\nu$ with $\nu = 3$.

We can also see from Figs. 13 and 14 that the regimes where the translational and rotational PN barriers for the triangular lattices with $\gamma = +1$ and $0 < C_2/C_1 < 1$ have similar magnitudes are approximately $0.25 \lesssim C_2/C_1 \lesssim 0.40$ for powers $1.5 \lesssim P/C_1 \lesssim 2.5$. Note also from Fig. 14 that the power thresholds go to zero as $C_2/C_1 \rightarrow 1/3$ as discussed in Sec. V B.

As for the square lattice, we also show a direct numerical illustration of rotational mobility and rotational PN barrier for a triangular lattice in Fig. 15. Note that the first barrier to overcome in this case corresponds to the unstable stationary solution rotated 30°, for which $|B_{m_0,j_0}|^2 = 3|A_{m_0,j_0}|^2$. Once this barrier has been overcome, the rotational velocity increases past the next stable stationary solution rotated 60°, with $|A_{m_0,j_0}|^2 = 3|B_{m_0,j_0}|^2$, slows down around the next unstable stationary solution rotated 90° (horizontal solution, $B_{m_0,j_0} = 0$), and so on. In this case, the difference between the theoretically estimated rotational PN barrier (1.8×10^{-3}, cf. Fig. 13) and the change of Hamiltonian for the threshold perturbation in Fig. 15 (7.5×10^{-3}) is larger and one may also observe in Fig. 15 small oscillations of the intensities on top of the rotational motion, indicating excitation of other modes carrying a non-negligible part of the Hamiltonian.

For comparison, we also show a direct numerical illustration of translational mobility and PN barrier for a triangular lattice in Fig. 16. In this case, as a norm-conserving perturbation which may initiate translation in the horizontal (strong-coupling) direction, we choose

$$A'_{m,j} = A_{m,j} \exp(-i\epsilon j),$$

$$B'_{m,j} = B_{m,j} \exp(-i\epsilon j). \qquad (17)$$

While the theoretically estimated translational PN barrier here is only 3×10^{-5} (cf. Fig. 14), the change of Hamiltonian for the threshold perturbation in Fig. 16 is 3×10^{-4} and it is evident that many other eigenmodes are also considerably excited by the perturbation (17). (For the example in Fig. 16,
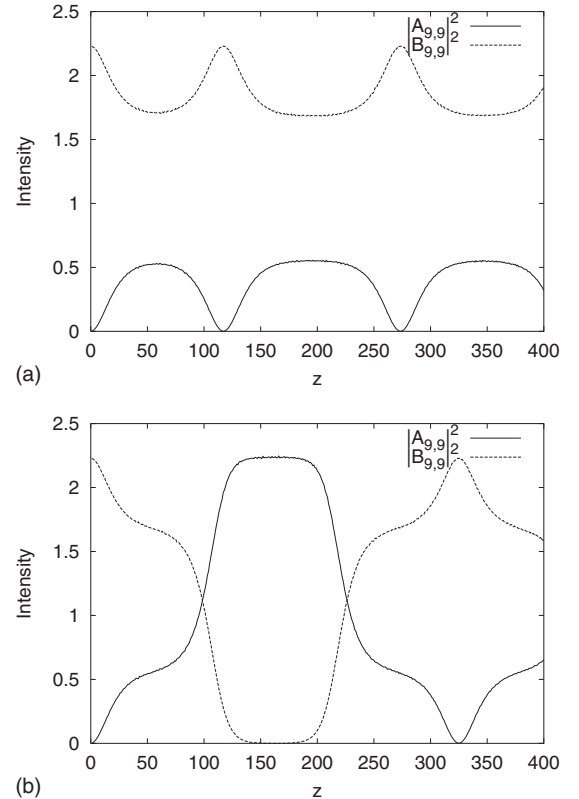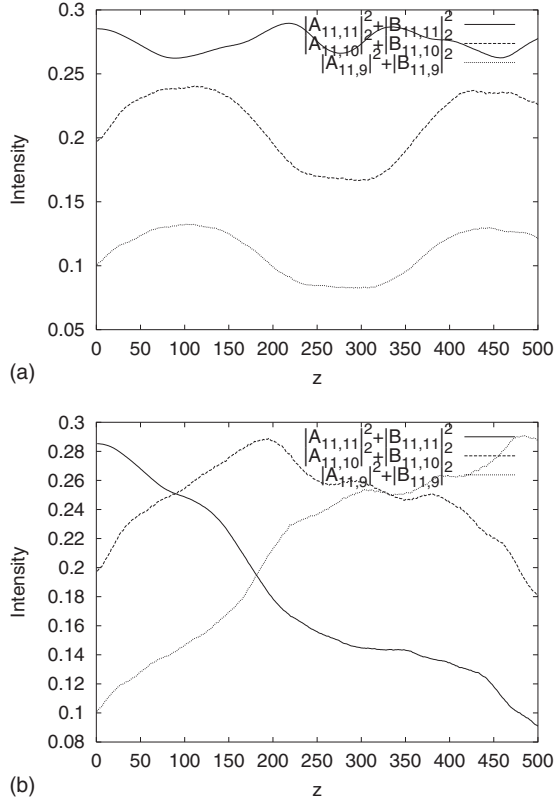

(a)

(b)

FIG. 15. Evolution along z for an initially perturbed stable one-site vertical dipole mode in a triangular lattice, with the same parameter values as in Fig. 13 but with $P=3$. Solid (dashed) lines show the A (B) parts of the central-site intensity. The perturbation is chosen from Eq. (16) with $\epsilon=0.0306$ (a) just below rotation threshold and $\epsilon=0.0307$ (b) just above rotation threshold. System size 17×17, periodic boundary conditions.

(a)

(b)

FIG. 16. Evolution along z for an initially perturbed stable one-site vertical dipole mode in a triangular lattice, with the same parameter values as in Fig. 13 but with $P \approx 1.149\,545$. Solid lines show the total intensity of the central site (11,11), dashed lines of its horizontal neighbor (11,10), and dotted line of its horizontal next-nearest neighbor (11,9). The perturbation is chosen from Eq. (17) with $\epsilon = 0.012$ (a) below translation threshold and $\epsilon = 0.014$ (b) above translation threshold. System size 21×21, periodic boundary conditions.

the solution also gets trapped after moving only two sites in the lattice.)

We finally discuss the triangular lattice with $\gamma = -1$ and $0 < C_2/C_1 < 1$. In this case, there is very poor translational mobility for the stable vertical dipole modes in all directions;
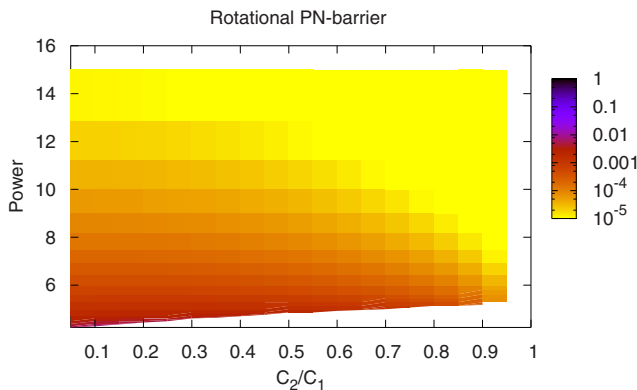
the translational PN barrier is then so large so it is not really a meaningful concept. We therefore only discuss the rotational PN barrier illustrated in Fig. 17. For most values of C_2/C_1, the barrier is monotonously decreasing to zero for increasing power, with exponent $\mu \approx 4$ for large power just as for $\gamma = +1$. However, a careful investigation reveals a more intricate behavior in the weak-anisotropy regime. Indeed, we know from Sec. V B that there is a small regime of stability inversion where the stable mode is not the vertical but the horizontal one. This reflects itself in the PN barrier, which becomes zero at the boundary of this regime. For example, when $C_2/C_1 = 0.95$, this regime appears at $P/C_1 \lesssim 5.23$ (the threshold power for this case is $P/C_1 \approx 5.18$).

Let us finally also remark that for the isotropic case, $C_2 = C_1$, the rotational PN barrier is identical for positive and negative γ but with opposite signs in its definition, since for $\gamma = +1$ the vertical mode is stable and for $\gamma = -1$ the horizontal one. In this case, the barrier decreases very rapidly to zero with increasing power. Although our numerical results here are not completely quantitatively conclusive due to the smallness of the barrier, they seem consistent with the hypothesis of a power-law decay with exponent $\mu = 11$ (corresponding to $\nu = 13/2$ according to Sec. V A).

VII. DISCUSSION AND CONCLUSIONS

In conclusion, our results reveal the essential properties of discrete optical solitons, which formed as collective excitations of dipole-guided modes in two-dimensional lattices of coupled optical waveguides. We have derived coupled-mode equations taking into account linear and nonlinear couplings between the dipole modes, which enabled us to establish the generic soliton properties. Our analysis reveals the existence, stability, and mobility characteristics of fundamental dipole-mode and vortex solitons in square and triangular lattices, providing deeper insight into previous numerical and experimental studies of such solitons [3–6]. Additionally, we have introduced a concept of "rotational Peierls-Nabarro barrier," which defines the minimum energy needed for rotation of stable dipole modes. We found that, in contrast to the commonly analyzed translation mobility, the rotational barrier
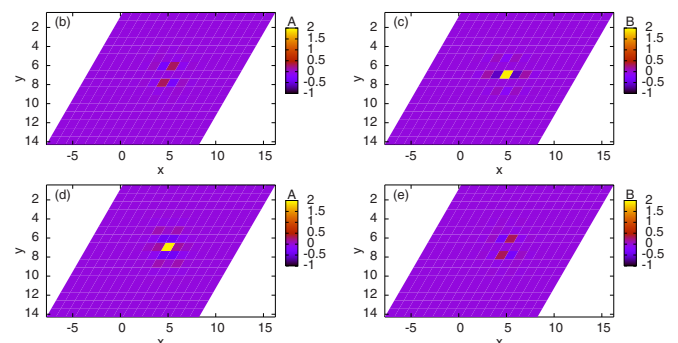

FIG. 17. (Color online) Left figure shows rotational PN barrier as a function of power and anisotropy ratio C_2/C_1 for a triangular lattice with $\gamma = -1$, $\sigma' = 1/3$, $C_1 = 1$, and other coupling constants given by Eq. (13). Only VK-stable modes are included. Right figures show A and B components of the modes used to calculate the PN barrier at $C_2 = 0.35$ and $P = 5$. [(b) and (c)] Stable one-site vertical dipole mode. [(d) and (e)] Unstable one-site horizontal dipole mode.

generally decreases for strongly localized states. These results suggest possibilities for controlling beam shaping in photonic lattices and waveguide arrays.

ACKNOWLEDGMENTS

[1] S. John and N. Aközbek, Phys. Rev. Lett. **71**, 1168 (1993).

[2] N. Aközbek and S. John, Phys. Rev. E **57**, 2287 (1998).

[3] R. Fischer, D. Träger, D. N. Neshev, A. A. Sukhorukov, W. Krolikowski, C. Denz, and Yu. S. Kivshar, Phys. Rev. Lett. **96**, 023905 (2006).

[4] C. R. Rosberg, D. N. Neshev, A. A. Sukhorukov, W. Krolikowski, and Yu. S. Kivshar, Opt. Lett. **32**, 397 (2007).

[5] O. Manela, O. Cohen, G. Bartal, J. W. Fleischer, and M. Segev, Opt. Lett. **29**, 2049 (2004).

[6] G. Bartal, O. Manela, O. Cohen, J. W. Fleischer, and M. Segev, Phys. Rev. Lett. **95**, 053904 (2005).

[7] Z. Q. Shi and J. K. Yang, Phys. Rev. E **75**, 056602 (2007).

[8] T. Dohnal, D. E. Pelinovsky, and G. Schneider, J. Nonlinear Sci. **19**, 95 (2009).

[9] Yu. S. Kivshar and G. P. Agrawal, *Optical Solitons: From Fibers to Photonic Crystals* (Academic Press, San Diego, 2003).

[10] J. Hudock, P. G. Kevrekidis, B. A. Malomed, and D. N. Christodoulides, Phys. Rev. E **67**, 056618 (2003).

[11] J. Meier, J. Hudock, D. Christodoulides, G. Stegeman, Y. Silberberg, R. Morandotti, and J. S. Aitchison, Phys. Rev. Lett. **91**, 143907 (2003).

[12] R. L. Horne, P. G. Kevrekidis, and N. Whitaker, Phys. Rev. E **73**, 066601 (2006).

[13] K. J. Blow, N. J. Doran, and D. Wood, Opt. Lett. **12**, 202 (1987).

[14] P. G. Kevrekidis, D. J. Frantzeskakis, R. Carretero-Gonzalez, B. A. Malomed, and A. R. Bishop, Phys. Rev. E **72**, 046613 (2005).

[15] J. Gómez-Gardeñes, L. M. Floría, and A. R. Bishop, Physica D **216**, 31 (2006).

[16] M. Johansson and Yu. S. Kivshar, Phys. Rev. Lett. **82**, 85 (1999).

[17] P. G. Kevrekidis, B. A. Malomed, and Y. B. Gaididei, Phys. Rev. E **66**, 016609 (2002).

[18] W. S. Duan, G. X. Wan, X. Y. Wang, and M. M. Lin, Phys. Plasmas **11**, 4408 (2004).

[19] W. S. Duan and M. M. Lin, Chaos, Solitons Fractals **28**, 1212 (2006).

[20] B. Farokhi, I. Kourakis, and P. K. Shukla, Phys. Lett. A **355**, 122 (2006).

[21] B. Farokhi, I. Kourakis, and P. K. Shukla, Phys. Plasmas **13**, 122304 (2006).

[22] Yu. S. Kivshar and D. K. Campbell, Phys. Rev. E **48**, 3077 (1993).